Robotica (2015) volume 33, pp. 107–126. © Cambridge University Press 2014
doi:10.1017/S026357471400006X

Regenerative effects in the Sit-to-Stand and Stand-to-Sit movement

Ronnie Joseph Wong* and James Andrew Smith

Department of Electrical and Computer Engineering, Ryerson University, Toronto, Ontario, Canada

(Accepted December 24, 2013. First published online: January 31, 2014)

SUMMARY

While Sit-to-Stand and Stand-to-Sit are routine activities and are crucial pre-requisites to walking and running their underlying dynamics are poorly understood. Furthermore, the potential for using these movements to regenerate energy in energy-sensitive devices such as orthoses, prostheses and humanoid robots has never been examined. Insights in this domain can lead to more energy-efficient prosthesis, orthosis and humanoid robot designs. *OBJECTIVES*: The objectives are two-fold: first, to determine how much energy can be regenerated during standard movements related to transitions between sitting and standing on a scale humanoid model and second, to determine if the chosen actuator could produce better results if the gear ratio were modified. This manuscript's main contribution to the literature is by showing which joint provides the most regenerative effect during transitions between sitting and standing. *MODEL DESIGN AND IMPLEMENTATION*: Joint trajectories from existing biomechanics trials of sitting and standing transitions were fed into a 1/10 scale model of a humanoid robot. The robot model, developed in MapleSim, is comprised of standard and off-the-shelf subcomponents, including amplifier, NiMH battery and Robotis Dynamixel RX-28 actuators. *RESULTS*: Using the RX-28 actuator, the ankle, knee and hip joints all show a degree of regenerative effects, the hip demonstrates the most dramatic levels during the transition from standing to sitting. This contrasts with recent publications which show that the knee has the most important regenerative effects during walking and running. It is also found that for under 3 degree trajectory error the regenerative effect is best for all joints when the gear ratio is increased from the RX-28's 193:1 value to a value of approximately 760:1 for the ankle, 630:1 for the knee and 600:1 for the hip. *CONCLUSIONS*: During transitions between sitting and standing the greatest potential for regeneration occurs in the hips. Therefore, systems designed to implement regenerative effects between sitting and standing need to include subsystems at the hip for maximum regenerative effects.

KEYWORDS: Bipeds; Control of robotic systems; Design; Exoskeletons; Humanoid robots; Human biomechanics; Legged robots; Biomimetic robots.

1. Introduction

The study of human, animal and robot locomotion has, in general, focused on steady-state aspects. However, in reality, steady-state locomotion is generally short-lived and is accentuated by frequent transitions between states. The aspects related to starting, turning, standing up, sitting down, accelerating and decelerating of everyday animal, human and now even robot locomotion is a key focus for contemporary research labs. The motion of sitting and standing up from a chair is appearingly simple but increasingly difficult with increasing age and declining health.

There are fundamental differences between natural actuators and artificial ones and if we are to develop artificial aides to assist in locomotory activities of people it is important to understand their limitations. Muscle weaknesses, diseases and disabilities such as Parkinsons disease and strokes can lead to declining functional mobility and health in the aging population. An inability to develop sufficient joint torques in the lower extremities can increase the risk of falling[1] and hip fractures.[2]

* Corresponding author. E-mail: r25wong@ryerson.ca

Inspired by observations from biomechanics, researchers have developed a wide range of devices to mimic human movements or to assist human movements. Synthesizing human motion on a humanoid robotic platform allows us to study and better understand the dynamics of this motion and to develop and test new assistive devices. Assistive devices were mostly passive in nature until the advent of the popular Ottobock C-Leg in 1985. Typically, devices to help raise or lower people with mobility problems tend to be large and are often a fixture of a room (such as those found in hospitals or pools).[3] A range of new orthotic devices, which contain active components[4] are now being developed. Furthermore, there is interest in both assistive device and humanoid robot communities to develop energy efficient devices, sometimes inspired by technologies such as the Toyota Prius hybrid vehicle that uses regenerative braking. Regenerative power collects power from the motor during braking and reuses it with the objective of improving the energy utilization of the machinery or system. The conservation and renewability of power is a necessary design consideration for electrical devices which operate on modular battery power. These considerations make regenerative systems an attractive addition to active orthoses designs.[5]

This paper introduces regenerative braking technology towards increasing battery autonomy in active prostheses, orthoses and humanoid robotic design. We first outline our procedure for generating the trajectory of the Sit-to-Stand-Sit movement. After reviewing the biomechanical data, we will discuss how inverse dynamics were applied to develop a nonlinear torque controller to generate the required joint torques at the ankle, knee and hip to closely match the human kinematic motion. In order to investigate regions for regeneration during sitting and standing, an electromechanical subsystem consisting of a commercially available actuator, a DC-to-DC bridge converter and a battery model is modeled and placed at each of the ankle, knee and hip joints. Next, we import the Sit-to-Stand-to-Sit trajectory data into a 1/10-scaled robotic model. Finally, we analyze regions for regenerative recovery in the Sit-to-Stand (Si2St) and Stand-to-Sit (St2Si) movement.

2. Sit-to-Stand Robot

This section describes the kinematics, dynamics and MapleSim components used to create the simulation model.

2.1. Kinematic model

A review of literature on biomechanical research show that computer models often use sagittal plane symmetry and one leg in simulations.[10,15–18] To simplify analysis, our model is based on a simplified approach that restricts movement in the sagital plane. The eventual goal is to implement the model in a small robot using the Robotis RX-28 off-the-shelf actuator. This constrains our design to a 1/10 scale. Kinematic parameters for the model were extracted from Roebroeck *et al.*[8] and scaled down to 1/10 using Winter's[19] anthropometric segment ratios.

Two simulation models were developed. The first model features a ground-fixed, bilateral contact ankle while the second model features a foot with two unilateral ground contact points (heel and ball of foot). Since foot movement is not required or moves very little in the Si2St and St2Si movement, the first model reduces the complexity in generating the dynamics equations by solving the system as a three-segment, three revolute inverted pendulum model[20] where the ankle is fixed to the ground (i.e. no foot). This model has three actuated degrees of freedom.

Our second computer, model is unhinged from the ground and two unilateral ground contact models are added to represent the foot (heel and ball of foot contact points) as shown in Fig. 1. The foot mass m_0 is added to the model to account for the total projected COM over the foot. Table I summarizes the variables listed in the figure. This allows us to test the stability of the model for a given trajectory dataset without increasing the complexity in the degrees of freedom. The model will fall over if the body center-of-mass (COM) lies outside the region of stability above the foot. Fig. 2 shows the projected ground COM arrow while sitting.

2.2. Trajectory generation

Successful motion without falling of the sit-to-stand and stand-to-sit movement requires an accurate knowledge of the robot's center-of-mass.[6] If the body center-of-mass is outside the region of stability (above the feet), stability is lost and the robot will fall. The movement can be considered quasi-static. There has been extensive research on lower extremity kinematics of the sit-to-stand and

https://doi.org/10.1017/S026357471400006X Published online by Cambridge University Press

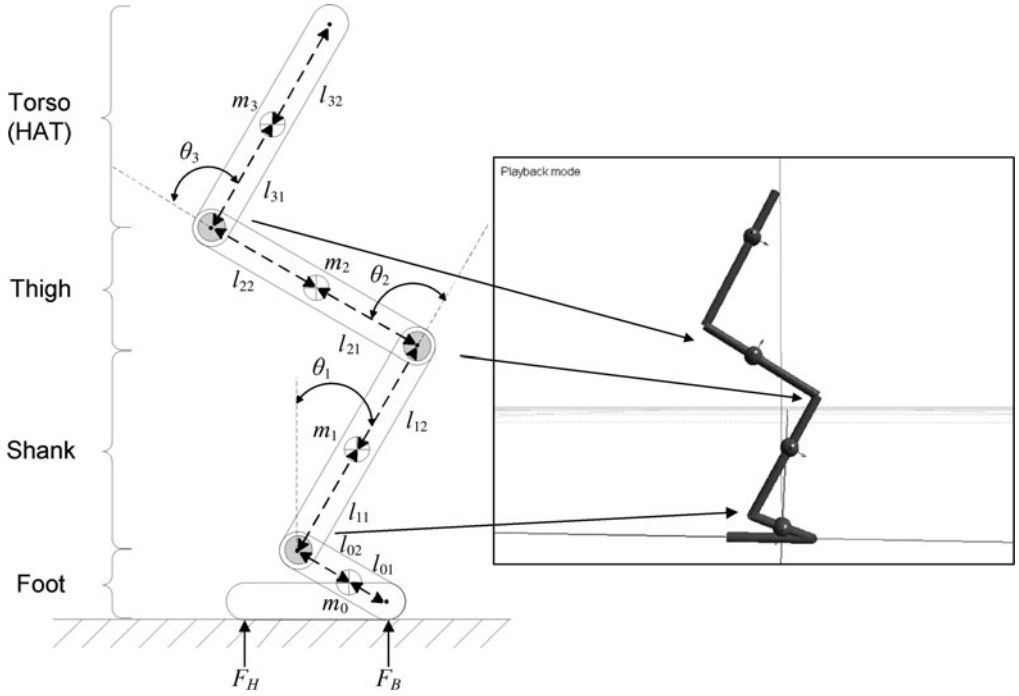

Fig. 1. Kinematic biomimetic robot model with foot, three actuated joints and two points of contact between foot and ground.

Table I. MapleSim three-segment, three-revolute inverted pendulum parameters.

Parameter	Description	Unit
θ_1	Ankle angle	[deg .]
θ_2	Knee angle	[deg .]
θ_3	Hip angle	[deg .]
m_0	Foot mass	[kg]
m_1	Shank mass	[kg]
m_2	Thigh mass	[kg]
m_3	Head,arms,trunk (HAT) mass	[kg]
l_{01}	Lower foot segment length	[m]
l_{02}	Upper foot segment length	[m]
l_{11}	Lower shank segment length	[m]
l_{12}	Upper shank segment length	[m]
l_{21}	Lower thigh segment length	[m]
l_{22}	Upper thigh segment length	[m]
l_{31}	Lower HAT segment length	[m]
l_{32}	Upper HAT segment length	[m]
F_H	Foot heel force	[N]
F_B	Foot ball force	[N]

sit-to-stand-to-sit[7–13] movements. There has generally been more focus on the sit-to-stand movement as it is a prerequisite for gait (like walking and running). The sit-to-stand-to-sit movement requires greater control effort during the sit-down phase. Sitting down requires more joint and muscle control since the person is generally not looking at his/her approach towards the chair.

From the available literature, Kralj *et al.*[14] published the clearest sit-to-stand-to-sit joint trajectory profile figures. We extracted trajectory data for the ankle, knee and hip using a digitizing software. A Matlab dataplot showing the extracted trajectories is shown in Fig. 3. Robot stability for this data is verified by the model not falling over during simulation.

https://doi.org/10.1017/S026357471400006X Published online by Cambridge University Press

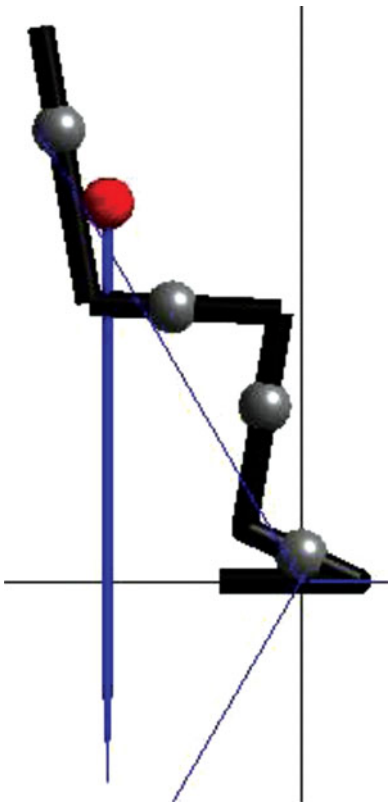

Fig. 2. (Colour online) Robot model based on anatomical data[19] scaled by 1/10, shown here sitting on a virtual chair, with the centre of mass and a line showing its projection towards the ground.

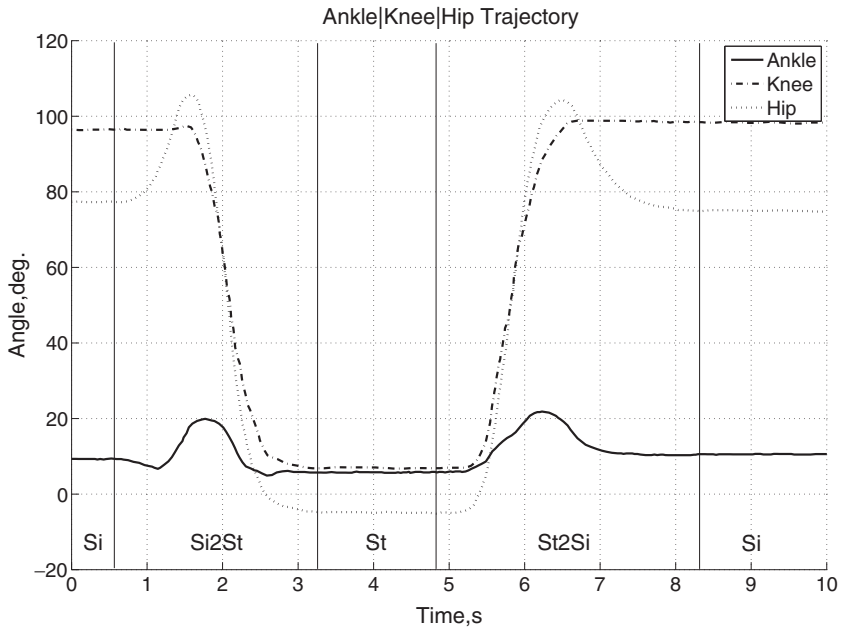

Fig. 3. Matlab plot data derived from Kralj *et al.*[14] illustrating the ankle, knee and hip joint trajectories, starting with a sit, transitioning to a stand and back to a sit. The data is taken from real human trials and forms the desired trajectories for the simulations described here.

https://doi.org/10.1017/S026357471400006X Published online by Cambridge University Press

2.3. Dynamics model

A mathematical model defining the dynamics of the biomechanical model is essential to the study of joint control. The equations of motion were generated for a fixed-ankle model. This assumes that foot movement is negligible during the Si2St and St2Si movements and therefore behaves as a three-segment, three-revolute inverted pendulum. To simplify analysis, we have ignored friction and disturbances that are non-rigid-body related. The rigid-body dynamics have the form

$$\boldsymbol{\tau} = \boldsymbol{M}(\boldsymbol{\theta})\ddot{\boldsymbol{\theta}} + \boldsymbol{V}(\boldsymbol{\theta}, \dot{\boldsymbol{\theta}}) + \boldsymbol{G}(\boldsymbol{\theta}), \tag{1}$$

where $\boldsymbol{M}(\boldsymbol{\theta})$ is the $\mathbf{n} \times \mathbf{n}$ mass matrix of the three-segment, three-revolute arm, $\boldsymbol{V}(\boldsymbol{\theta}, \dot{\boldsymbol{\theta}})$ is an $n \times 1$ vector of centrifugal and Coriolis components, and $\boldsymbol{G}(\boldsymbol{\theta})$ is an $n \times 1$ vector of gravitational components.The mass matrix is represented by a 3×3 system of the form

$$\boldsymbol{M}(\boldsymbol{\theta}) = \begin{bmatrix} \alpha_1 & \alpha_2 & \alpha_3 \\ \beta_1 & \beta_2 & \beta_3 \\ \gamma_1 & \gamma_2 & \gamma_3 \end{bmatrix}, \tag{2}$$

where the 3×1 vector of centrifugal and Coriolis components is of the form

$$\boldsymbol{V}(\boldsymbol{\theta}, \dot{\boldsymbol{\theta}}) = [\delta_1 \;\; \delta_2 \;\; \delta_3]^T \tag{3}$$

and the 3×1 vector of gravitational components is of the form

$$\boldsymbol{G}(\boldsymbol{\theta}) = [\zeta_1 \;\; \zeta_2 \;\; \zeta_3]^T. \tag{4}$$

The expanded form for Eqs. (2)–(4) can be found Appendix A.

2.4. Nonlinear torque controller

The open loop model in Eq. (1) is a multi-input, multi-output type problem. The system has a vector of desired joint positions, velocities and accelerations and the control law must calculate a vector of joint actuator signals that are tightly coupled together. The control law is based on the convention outlined in Craig[20] [pp. 262–316] where the controller will be partitioned into a model-based portion and a servo-based portion. The model-based portion is of the form

$$\boldsymbol{\tau} = \boldsymbol{\alpha}\, \boldsymbol{\tau}' + \boldsymbol{\beta}, \tag{5}$$

where τ, τ' and β are 3×1 vectors and α is a 3×3 matrix. For our rigid-body model, the open loop equation of motion is of the form

$$\boldsymbol{\tau} = \boldsymbol{M}(\boldsymbol{\theta})\ddot{\boldsymbol{\theta}} + \boldsymbol{V}(\boldsymbol{\theta}, \dot{\boldsymbol{\theta}}) + \boldsymbol{G}(\boldsymbol{\theta}). \tag{6}$$

We choose α and β to be

$$\boldsymbol{\alpha} = \boldsymbol{M}(\boldsymbol{\theta}), \tag{7}$$

$$\boldsymbol{\beta} = \boldsymbol{V}(\boldsymbol{\theta}, \dot{\boldsymbol{\theta}}) + \boldsymbol{G}(\boldsymbol{\theta}). \tag{8}$$

Again, equating Eq. (6) with Eq. (5) reduces the system to appear as an identity mass matrix for τ'

$$\boldsymbol{\tau}' = \boldsymbol{I}\, \ddot{\boldsymbol{\theta}}. \tag{9}$$

https://doi.org/10.1017/S026357471400006X Published online by Cambridge University Press

The identity mass matrix has units in $kg \cdot m^2$. The servo-based portion of the control law is

$$\boldsymbol{\tau}' = (\ddot{\boldsymbol{\theta}}_d + \boldsymbol{K}_v \dot{\boldsymbol{E}} + \boldsymbol{K}_p \boldsymbol{E})\boldsymbol{I}, \tag{10}$$

where the 3×1 angular position error matrix $\boldsymbol{E}$ is defined as

$$\boldsymbol{E} = \theta_d - \theta \tag{11}$$

and $\dot{\boldsymbol{E}}$ is the 3×1 angular velocity error matrix. Equating Eq. (9) with Eq. (10) results in the characteristic error equation

$$0 = \ddot{\boldsymbol{E}} + \boldsymbol{K}_v \dot{\boldsymbol{E}} + \boldsymbol{K}_p \boldsymbol{E}, \tag{12}$$

where the gain vectors K_v and K_p are diagonal 3×3 matrices. The nonlinear joint torque controllers for the ankle (θ_1), knee (θ_2) and hip (θ_3) can be realized by expanding Eqs. (10) and (5).

2.5. Ground contact model

Any robot or humanoid model focused on leg-based movements needs to include a model of the interaction between the feet and the ground.[21,22] A unilateral ground contact model is incorporated to verify the lower extremity joint motions meet stability during the Si2St2Si motion. It effectively unhinges the foot from the ground and introduces instability and tipping of the model if the total body COM is not within the region of stability during the Si2St2Si motion. A stable Si2St2Si transition is realized by the total body COM over the foot as shown in Fig. 4. The model is referenced with respect to a Cartesian coordinate system where the x-plane is parallel to the foot and the z-plane is vertical and orthogonal to the x-plane. The ground contact model in the simulation was modified from Dr. Gilbert Lai's (MapleSim) simulation on a rotating rimless wheel.[23] The surface friction relationship is

$$F_{friction} = (-K_d) \cdot \dot{x}, \tag{13}$$

where K_d is the viscous damping coefficient with units of $N \cdot s/m$ and $\dot{x}$ is in ms^{-1}. The normal force relationship is

$$F_{normal} = K_p \cdot z + K_d \cdot \dot{z}, \tag{14}$$

where K_p and K_d are spring and damping coefficients with units of N/m and $N \cdot s/m$ and z and $\dot{z}$ have units of m and ms^{-1}. K_p and K_d were manually tuned to be $2 \times 10^{11} N/m$ and $1.5 \times 10^{11} N \cdot s/m$.

2.6. Joint actuator subsystem

One of the objectives of the study is to provide an accurate simulation of hardware components for use in a future robot. Therefore, it is important to model the simulation with actual hardware parameters (such as motor terminal inductance, resistance and stall torque) that will generate similar performance values between hardware and software. For a regenerative braking circuit, the major components are the actuator, battery and H-bridge. It allows us to investigate the energy usage and recovery during specific phases of the Si2St2Si movement. Regenerative braking refers to using the power associated with the counter electromotive force (CEMF) voltage of an electric motor to charge a battery. In normal operation mode, the battery is used to provide positive power to an electric motor. In braking, the electric motor acts as a generator and negative power assists in injecting energy back into the battery. Permanent magnet DC motors can operate in four quadrants. Four quadrant operation refers to the four possible regions that a dc motor can operate in ref. [24]. Two of the four regions allow for positive power and will therefore drain the battery. The other two regions will generate negative power and will therefore recharge the battery. This section describes the components in the actuator subsystems that engages regeneration in ankle, knee and hip.

2.6.1. Dynamixel RX-28 actuator. Actuation of the lower limb joints of the robot model will require electrical actuators capable of generating the required trajectory torques and angular speeds. Our 1/10-scale robot model experiences the largest moment force at the knee during initial chair lift-off.

https://doi.org/10.1017/S026357471400006X Published online by Cambridge University Press

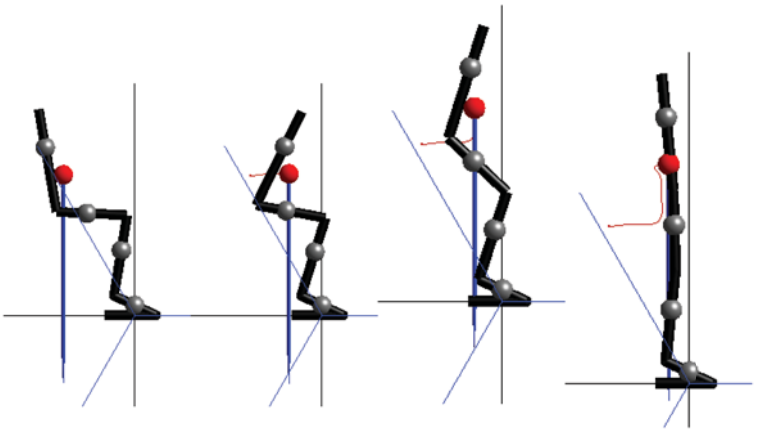

(a) Frame 1 ($t = 0$ s) (b) Frame 2 ($t = 1.6$ s) (c) Frame 3 ($t = 2$ s) (d) Frame 4 ($t = 3$ s)

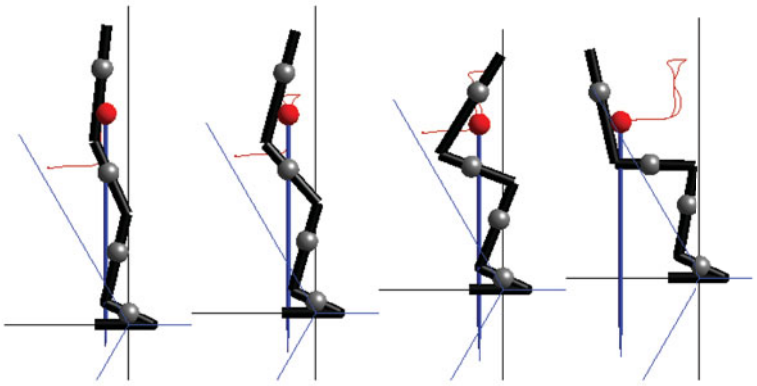

(e) Frame 5 ($t = 5.5$ s) (f) Frame 6 ($t = 6$ s) (g) Frame 7 ($t = 6.4$ s)(h) Frame 8 ($t = 9.5$ s)

Fig. 4. (Colour online) Typical motion of MapleSim Model performing Sit-to-Stand and Stand-to-Sit Motion. Trajectory of the Centre of Mass (COM) is shown, as is the ground-projected COM (gCOM).

The maximum knee torque for the 1/10-scaled model was calculated to be 0.22 Nm assuming that chair lift-off is 90 degrees. The maximum angular velocity amongst the joints is located at the hip and measured to be approximately 100 deg/s (or 1.75 rad/s).[8] One of our objectives was to develop a low-cost off-the-shelf prototype to study regenerative braking feasibility towards lower extremity orthosis/prothesis applications. To meet this requirement, we used existing components in the lab. The Dynamixel RX-28 actuator is a high performance digital servo that is used in academic research labs worldwide.[25–27]

The RX-28 actuator was modeled in MapleSim. MapleSim discrete components were used to model standard electromechanical equations that describe the internal permanent magnet DC motor.[24] To develop the actuator, electrical and mechanical parameters of the Maxon motor inside the RX-28 were required. However, Robotis and Maxon Motors have made this information proprietary. To determine the motor parameters, we extracted the motor from its plastic casing to measure its physical dimensions. The nameplate number on the motor was 275338. A Procise Vernier caliper (model #: 0121230)[28] was used to measure the dimensions of the motor. The diameter was measured to be 17 mm with a length of 25.2 mm. The mass of the motor was measured to be 0.026 kg using a Starfrit 93016 digital scale.[29] The terminal inductance and resistance of the motor were each measured three times and averaged with a Wavetek Meterman LCR55 component tester.[30] The input-shaft no-load speed and stall torque was calculated to be 11580 rpm and 0.0144 Nm.[31] With the calculated no-load speed, stall torque, measured dimensions and measured electrical characteristics, the RX-28 motor was a close match to the Maxon RE-max 17, order number 214897[31] and is summarized in Table II. Maxon Motors nor Robotis will confirm the RE-max 17 and the name plate on the RX-28

https://doi.org/10.1017/S026357471400006X Published online by Cambridge University Press

Table II. Comparison between RX-28 and RE-max 17 maxon motors.

		RX-28 maxon motor	
Parameter	Maxon RE-max 17[31]	Calculated/Measured	Robotis[34,35]
Stall torque (shaft input)	0.0144 Nm	0.0144 Nm	3.63 Nm (gear output shaft)
No-load speed (shaft input)	11500 rpm (1204 rad/s)	11580 rpm (1212 rad/s)	8.90 rad/s (gear output shaft)
Nominal voltage	12.0 V	–	12.0 V
Start current	1.45 A	–	1.2 A
Terminal resistance	8.30Ω	8.55Ω (avg.)	n/a
Terminal inductance	0.206 mH	0.196 mH (avg.)	n/a
Motor diameter	17 mm	17.0 mm	n/a
Motor length	25.4 mm	25.2 mm	n/a
Motor weight	0.026 kg	0.026 kg	n/a
Nameplate data	214897	275338	n/a

motor does not match any known type in the current Maxon product catalog. Similar parameter studies on RX-28 motor determination have also concluded on the RE-max 17, order number 214897.[32,33]

2.6.2. NiMH battery model. Power must be delivered between the dc motor actuators and batteries during the Si2St2Si motion. For an unconstrained Si2St2Si rehabilitative device to be feasible for everyday use, the system must run on its own power supply. Many battery technologies exist in the industry to power various portable devices. Some of the more popular topologies include lead acid; nickel-metal hydride (NiMH); lithium polymer (LiPo) as well as lithium ion. To simplify analysis, our robotic model will use the common NiMH rechargeable battery supply. Our model will assume that the battery is capable of handling the recharge levels during regenerative braking without damage and therefore will not require any additional power conditioning circuitry.

Software-based battery modeling is an active area of research but until recently, has been limited to simple models that often do not adequately describe the complex chemical reactions in the battery. Accurate models have the benefit of predicting and optimizing the lifetime in battery performance. Given an applied load to a battery over a certain period, performance criteria such as state of charge (SOC) or knowing when battery failure occurs can be used to trade-off system performance for extending battery lifetime at the design stages of model development.

The MapleSim modeling library contains a battery model that is based upon the work by Dao *et al*.[36] This model accounts for the electrochemical processes and thermodynamic behavior of the NiMH battery and describes these equations as a set of equivalent electrical components interconnected to each other. The simulation uses a modified version of this model. It is based on a 4.5 Ahr battery made by North American Battery Company (NABC). The battery data was measured at A&D Technology's laboratory in Ann Arbor, Michigan, USA.[36]

2.6.3. H-Bridge: DC-to-DC converter. Electrical power transfer between the NiMH battery and the RX-28 is handled by the H-Bridge DC-to-DC converter. The H-Bridge model is a modified version of a DC-to-DC bridge converter that is available on MapleSim's website.[37] The functional block diagram for the continuous-time domain model is shown in Fig. 5. A voltage source signal delivers power to the RX-28 actuator. The power sensor then takes measurements per time step from the RX-28 and a voltage sensor measures the voltage across the battery terminals and this value is divided by the power sensor reading to determine the current draw and direction on the battery. This determines whether the battery is recharging or discharging.

3. Simulation

This section describes the regenerative effects during the sit-to-stand-to-sit movement. The analysis is done for a 1/10 scale robot model powered by 18.1V batteries and using the stock Dynamixel

https://doi.org/10.1017/S026357471400006X Published online by Cambridge University Press

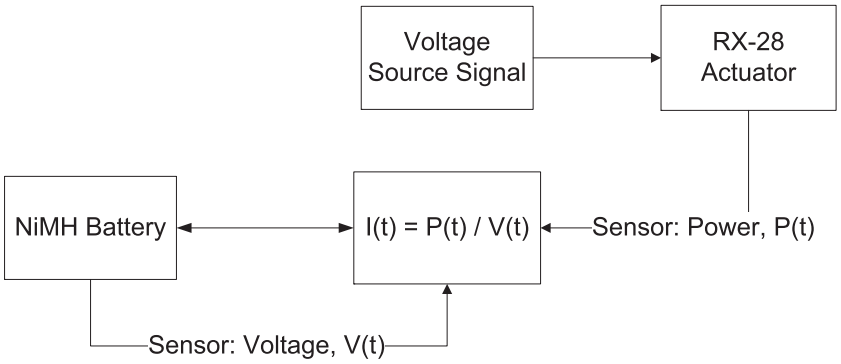

Fig. 5. Functional block diagram for the MapleSim H-Bridge DC-to-DC Converter.

RX-28 (193:1 gear ratio). The joint kinematics and dynamics were described in Section 2 and are based on ground-fixed, bilateral contact ankle since feet movement is not required or moves very little in the Si2St and St2Si movement. The simulation model used in this section is based upon the second computer model (Section 2) where it is unhinged from the ground using two unilateral ground contact models to represent the heel and ball of foot, as shown in Fig 1.

3.1. Simulated robot mimicking human movements

We evaluated our model in simulation using MapleSim 5. The model is initialized sitting on a virtual chair with contact occuring at the thigh. After each simulation, the data is exported from MapleSim and imported into Matlab for processing. A series of screenshots from a typical simulation is shown in Fig. 4. The ground projected center of mass (gCOM) extends from the system's overall COM. Given that the gCOM is behind the foot in Frame 1, if the chair was not present, the model would fall over. From Frames 2 - 4, the model rises from the chair. This is the Sit-to-Stand (Si2St) movement. The gCOM moves towards the foot to prevent tipping over. The trajectory of the system's COM is traced in space as the model moves. For Frames 5-8, the model sits down again (St2Si). As the model contacts the seat, the gCOM leaves the foot region. The trajectory of the COM for both Si2St and St2Si is visible in Frame 8.

3.2. Results

A multi-domain simulation model in MapleSim was developed and tested using the joint trajectories from Kralj *et al.*.[14] Here we show that regeneration can increase the autonomy of the robot model.

3.2.1. Regeneration using the RX-28 on a scale model. Here, we examine the use of the off-the-shelf RX-28 actuator, applied to a scale humanoid model during biomechanically-accurate sit-to-stand and stand-to-sit motions. State-of-charge (SOC) is an indicator on the capacity of a battery (0% = empty and 100% = full). Figure 6 shows the SOC deviation plotted against time for one sit-to-stand-to-sit cycle (10s) at the ankle, knee and hip. The SOC deviation is 0 at initial start time with a full SOC state level of 0.8. From this figure, we can see that the SOC deviation increases over time which indicates power being drawn from the battery. There is a larger load on the subsystem with regeneration-disabled. At approximately 6s, we can see that regeneration helps extend battery autonomy by increasing the SOC level. As seen in the figures, the ankle and knee subsystems showed very little regeneration compared to the hip. The figures also indicate that regeneration is more prominent during the stand-to-sit phase.

In Fig. 7, we compare the electrical power on the battery and SOC deviation over time. We can see that regeneration occurs around 2 s with the greatest amount of regeneration occuring around 6 s at the hip. In the beginning of the sit-to-stand movement, the body moves the torso forward through actuation at the hip, effectively shifting the body COM over the foot. Once the projected COM of the body is above the foot (approx. 2 s), the hip therefore begins braking. Braking at the hip also occurs around 6 s as the body maintains its project COM over the foot during the sit-down motion.

We see that regeneration recovery is relatively small between regeneration and no-regeneration simulations. This can be explained by the relatively large battery of 4.5Ahr used in the model. The

https://doi.org/10.1017/S026357471400006X Published online by Cambridge University Press

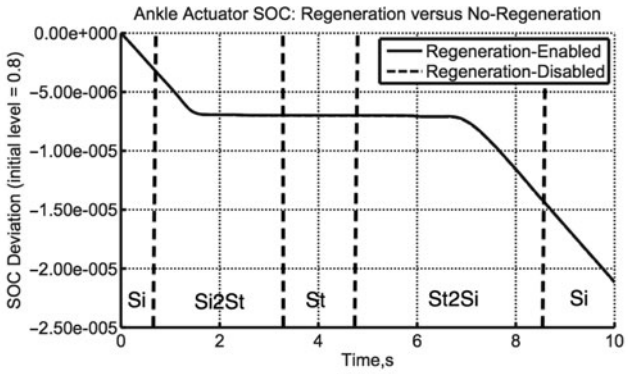

(a) Ankle joint actuator

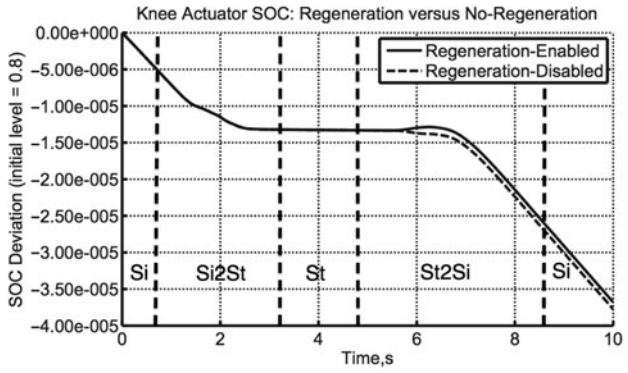

(b) Knee joint actuator

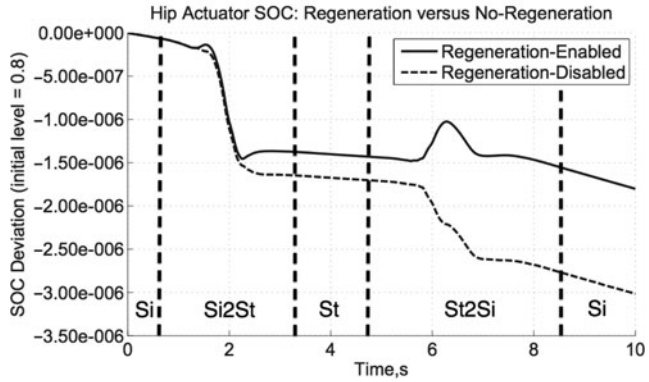

(c) Hip joint actuator

Fig. 6. Regeneration-enabled versus regeneration-disabled SOC Deviation comparison (193:1 Gear Ratio, 18.1V, 4.5 Ahr NiMH Battery). The initial state of the SOC level is 0.8 at time = 0 s.

peak current draw was found to be 0.25A with an average current draw of approximately 0.05A. Although the simulation times per movement cycle lasted 10 s, total time for actual movement is approximately 6 s. It takes approximately 2.1 s to complete the sit-to-stand motion and 2.5 s for the stand-to-sit motion.

3.2.2. Trajectory tracking threshold from gear ratio performance. While the RX-28 actuator was chosen because it is commonly used in robots of the scale described in this paper, its gear ratio was found to yield only moderate regeneration results. To determine the maximum gear ratio for a desired tracking error a parameter sweep of the gear ratio was conducted, the results of which are shown in Figs. 8 and 9. Since Berkeimeir *et al.*[48] described a similar real Acrobot robot to have a maximum

https://doi.org/10.1017/S026357471400006X Published online by Cambridge University Press

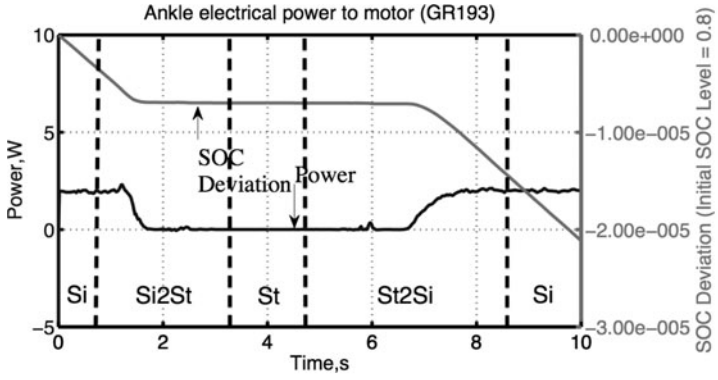

(a) Ankle: electrical motor power and SOC, 193:1 gear

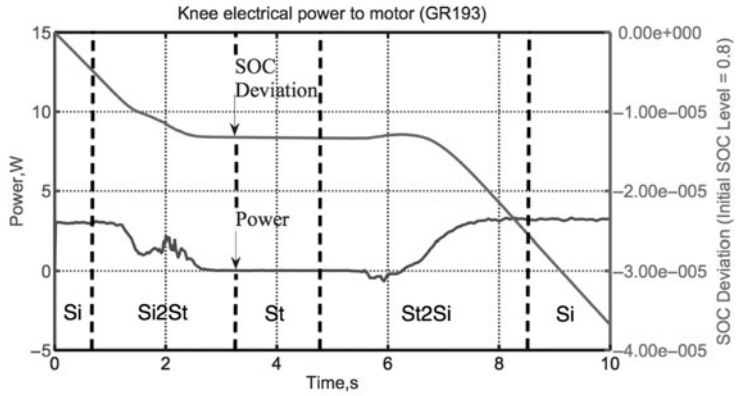

(b) Knee: electrical motor power and SOC, 193:1 gear

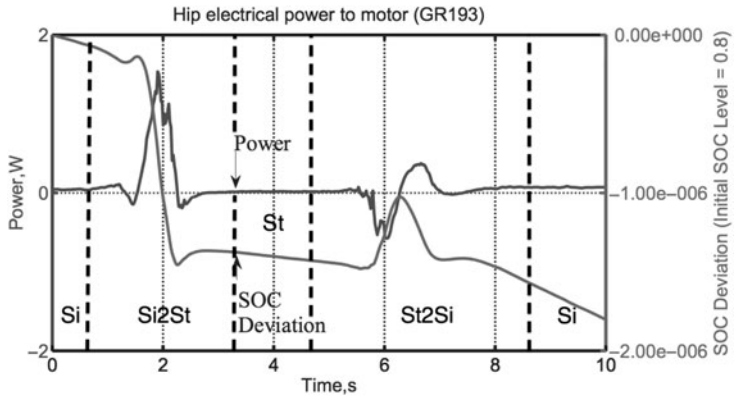

(c) Hip: electrical motor power and SOC, 193:1 gear

Fig. 7. Motor electrical power and SOC Performance using the RX-28 193:1 gear ratio. The initial state of the SOC level is 0.8 at time = 0 s.

3 degree trajectory error when performing similar movements we have set 3 degrees as the maximum acceptable error for all three joint trajectories. As shown in Fig. 8, the RX-28's 193:1 gear ratio of the RX-28 performs far worse for the regenerative task than a gear ratio of between 500:1 and 800:1. This applies to all three joints. Furthermore, tracking errors for various gear ratios shown in Fig. 9 show that the maximum acceptable trajectory tracking error (3 degrees) occurs at approximately 760:1 for the ankle, 630:1 for the knee and 600:1 for the hip. At these values, the percent decrease in SOC

https://doi.org/10.1017/S026357471400006X Published online by Cambridge University Press

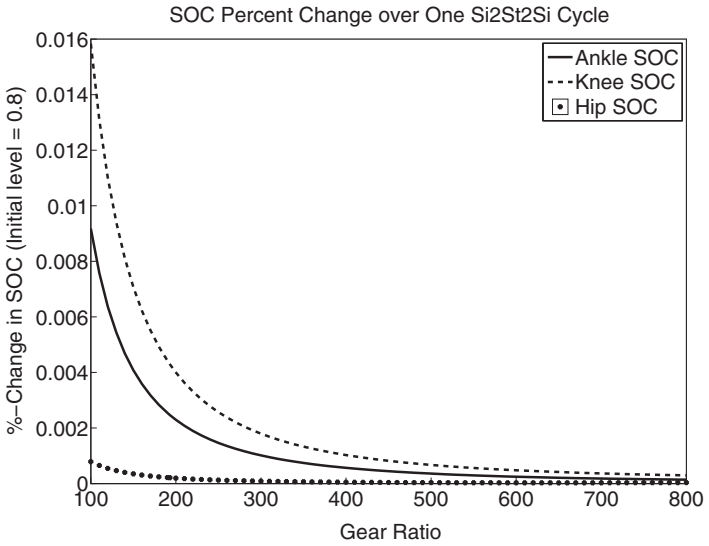

Fig. 8. Percent-change in SOC per Gear Ratio after one Si2St2Si cycle. The hip joint has consistently better (lower) reductions in state of charge, no matter the chosen gear ratio.

(initial level of 0.8) is $1.49 \times 10^{-4}\%$ for the ankle, $4.38 \times 10^{-4}\%$ for the knee and $2.64 \times 10^{-5}\%$ for the hip joint.

3.2.3. Discussion. Here we have presented work which applies a nonlinear torque control strategy for an actuated Si2St2Si biped model that mimics joint trajectories from human biomechanics trials. This was achieved by developing a multi-domain simulation model in MapleSim. There has been extensive research on regeneration capturing in running and walking but never on Si2St2Si.[40–47] The study has led to a better understanding on the potential for regeneration in Si2St2Si motion and trajectory regions where regeneration and optimization should be focused on. In walking and running cases, it has been shown that maximum energy recovery is obtained at the knee.[38,39] In contrast to this other work, we find here that it would be most effective if placed at the hip for sitting/standing behaviors.

While the original goal was to use an off-the-shelf actuator with a fixed gear ratio of 193:1, our analysis shows that the system can have better regenerative recovery and motion tracking if gear ratios closer to 760:1 for the ankle, 630:1 for the knee and 600:1 for the hip are chosen. The simulation using these new gear ratios showed the joint trajectory errors were below the maximum tolerance of 3 degrees. In summary, the study shows that regeneration and motor braking can be used to assist the Si2St2Si behavior. It was shown that regeneration during negative cycles extended the operational time by injecting energy back into the battery. Battery autonomy was therefore increased, extending the operation time of the device. This in return can help reduce joint loads during standing-to-sitting for the user. We recommend that the hip joint be prioritized for regeneration since the ankle and knee show less potential for useful regenerative effects. The increase in battery autonomy due to regeneration and gearing can lead to designs with smaller, lighter batteries. This has important implications for prostheses, orthoses and humanoid robot design.

4. Conclusion

The objectives of this paper are to determine how much energy can be regenerated during standard movements related to transitions between sitting and standing on a scale humanoid model as well as to determine if the chosen actuator could produce better results if the gear ratio were modified. While there has been extensive research on regeneration capturing in running, our work is novel in that it specifically examines theses effects in transitions between sitting and standing. To accomplish this trajectories of human sit-to-stand and stand-to-sit trials were fed into a 1/10 scale model of a humanoid robot developed in MapleSoft MapleSim. The ankle, knee and hip joints all show a degree of regenerative effects. In contrast to work by Donelan[38,39] where regenerative technology is

https://doi.org/10.1017/S026357471400006X Published online by Cambridge University Press

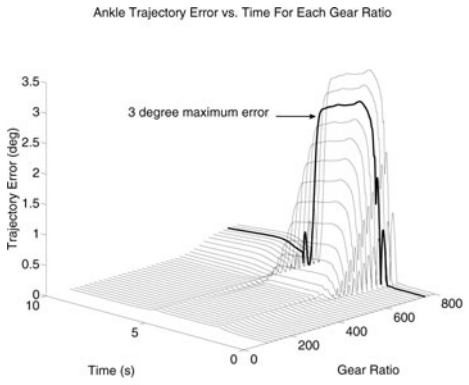

(a) Ankle joint tracking error

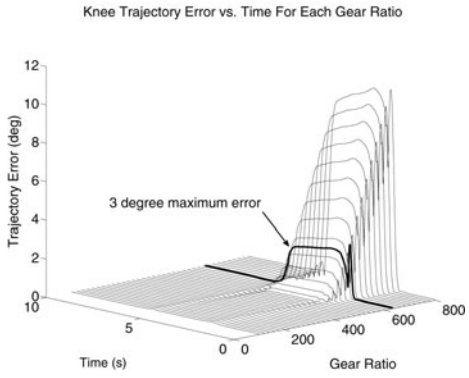

(b) Knee joint tracking error

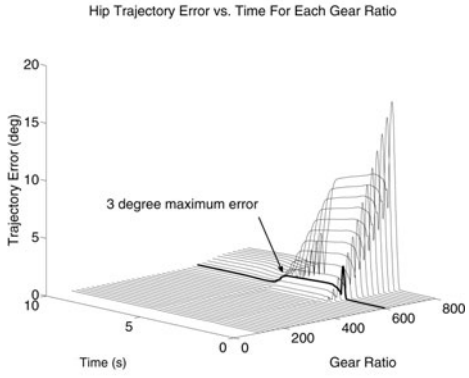

(c) Hip joint tracking error

Fig. 9. Joint Tracking Error for gear ratios 100:1 to 800:1 (18.1V, 4.5 Ahr NiMH). The trajectories for which gear ratios (760:1 for the ankle, 630:1 for the knee and 600:1 for the hip) have error not exceeding three degrees is shown with a thicker line.

applied at the knee for walking and running, here the hip demonstrates the most dramatic levels of regeneration during the transition from standing to sitting.

Using this approach the modeled battery autonomy was increased, extending the operation time of the device. This in return has the potential to help reduce joint loads during standing-to-sitting for prosthesis or orthosis users. We recommend that the hip joint be prioritized for regeneration since the ankle and knee show less potential for useful regenerative effects. The increase in battery autonomy due to regeneration and gearing can lead to designs with smaller, lighter batteries. This has important implications for prostheses, orthoses and humanoid robot design.

https://doi.org/10.1017/S026357471400006X Published online by Cambridge University Press

References

1. W. G. Janssen, H. B. Bussmann and H. J. Stam, "Determinants of the sit-to-stand movement: a review," *Phys. Ther.* **82**(9), 866–879 (2002).
2. Canada. Public Health Agency of Canada, *The chief public health officers report on the state of public health in canada, 2010: Growing older-adding life to years*. [Online]. Available at: http://www.phac-aspc.gc.ca/cphorsphc-respcacsp/2010/fr-rc/index-eng.php. (accessed April 10, 2011).
3. R. Kamnik and T. Bajd, "Human voluntary activity integration in the control of a standing-up rehabilitation robot: A simulation study," *Med. Eng. Physi.* **29**(9), 1019–1029 (2007).
4. R. Kobetic, C. S. To, J. R. Schnellenberger, M. L. Audu, T. C. Bulea, R. Gaudio, G. Pinault, S. Tashman and R. Triolo, "Development of hybrid orthosis for standing, walking, and stair climbing after spinal cord injury," *J. Rehabil. Res. Dev.* **46**(3), 447–462 (2009).
5. G. Luo, Z. Chen, Y. Deng, M. Dou and W. Liu, "Research on Braking of Battery-Supplied Interior Permanent Magnet Motor Driving System," *Vehicle Power and Propulsion Conference, 2009. VPPC '09. IEEE* (2009) pp. 270–274.
6. M. Mistry, A. Murai, K. Yamane and J. Hodgins, "Sit-to-Stand Task on a Humanoid Robot from Human Demonstration," *Humanoid Robots (Humanoids), 2010 10th IEEE-RAS International Conference on* (2010) pp. 218–223.
7. C. A. Doorenbosch, J. Harlaar, M. E. Roebroeck and G. J. Lankhorst, "Two strategies of transferring from sit-to-stand; the activation of monoarticular and biarticular muscles," *J. Biomech.* **27**(11), 1299–1307 (1994).
8. M. Roebroeck, C. Doorenbosch, J. Harlaar, R. Jacobs and G. Lankhorst, "Biomechanics and muscular activity during sit-to-stand transfer," *Clin. Biomech.* **9**(4), 235–244 (1994).
9. K. Kerr, J. White, D. Barr and R. Mollan, "Analysis of the sit-stand-sit movement cycle in normal subjects," *Clin. Biomech. (Bristol, Avon)* **12**(4), 236 (1997).
10. S. Yoshioka, A. Nagano, R. Himeno, S. Fukashiro *et al.*, "Computation of the kinematics and the minimum peak joint moments of sit-to-stand movements," *Biomed. Eng. online* **6**, 26 (2007).
11. A. B. Schultz, N. B. Alexander and J. A. Ashton-Miller, "Biomechanical analyses of rising from a chair," *J. Biomech.* **25**(12), 1383–1391 (1992).
12. S. Nuzik, R. Lamb, A. VanSant and S. Hirt, "Sit-to-stand movement pattern a kinematic study," *Phys. Ther.* **66**(11), 1708–1713 (1986).
13. R. B. Shepherd and A. Gentile, "Sit-to-stand: Functional relationship between upper body and lower limb segments," *Hum. Mov. Sc.* **13**(6), 817–840 (1994).
14. A. Kralj, R. J. Jaeger and M. Munih, "Analysis of standing up and sitting down in humans: definitions and normative data presentation," *J. Biomech.* **23**(11), 1123–1138 (1990).
15. H. Hemami and V. C. Jaswa, "On a three-link model of the dynamics of standing up and sitting down," *IEEE Trans. Syst. Man Cybern.* **8**(2), 115–120 (1978).
16. P. D. Roberts and G. McCollum, "Dynamics of the sit-to-stand movement," *Biol. Cybern.* **74**(2), 147–157 (1996).
17. M. K. Mak, O. Levin, J. Mizrahi, C. W. Hui-Chan *et al.*, "Joint torques during sit-to-stand in healthy subjects and people with parkinsons disease," *Clin. Biomech. (Bristol, Avon)* **18**(3), 197–206 (2003).
18. R. Davoodi and B. J. Andrews, "Computer simulation of fes standing up in paraplegia: A self-adaptive fuzzy controller with reinforcement learning," *IEEE Trans. Rehabil. Eng.* **6**(2), 151–161 (1998).
19. D. A. Winter, *Biomechanics and Motor Control of Human Movement* (John Wiley & Sons, 2009).
20. J. J. Craig, *Introduction to Robotics: Mechanics and Control* (Prentice Hall, 2004).
21. M. H. Raibert *et al.*, *Legged Robots that Balance*, Vol. 3 (MIT press Cambridge, MA, 1986).
22. P. Holmes, R. J. Full, D. Koditschek and J. Guckenheimer, "The dynamics of legged locomotion: Models, analyses, and challenges," *Siam Rev.* **48**(2), 207–304 (2006).
23. G. Lai, "Rimless wheel," maplesoft.com. [Online]. Available at: http://www.maplesoft.com/applications/Category.aspx?cid=200&page=7 (2011) (accessed January 5, 2012).
24. N. Mohan, *Electric Drives: An Integrative Approach* (Minnesota Power Electronics Research & Education (MNPERE), 2003).
25. V. Tech, "Robotics & Mechanisms Laboratory (RoMeLa)," [Online]. Available at: http://www.romela.org/main/Robotics_and_Mechanisms_Laboratory (2011) (accessed January 15, 2012).
26. H.-U. zu Berlin, "Neurorobotics Research Laboratory," [Online]. Available at: http://www.neurorotik.de/index_en.php (2011) (accessed February 2, 2012).
27. M. University, "Robotics Center," [Online]. Available at: http://www.idt.mdh.se/rc/ (2012) (accessed January 15, 2012).
28. Procise, "Vernier Caliper," [Online]. Available at: http://www.rona.ca/shop/ caliper-vernier-procise-344760_hand-tools_shop (2011) (accessed January 10, 2012).
29. L. P. A. Inc., "Starfrit 93016 Electronic Scale," [Online]. Available at: http://www.starfrit.com/ (2011) (accessed January 10, 2012).
30. Meterman, "Component Testers (LCR55,CR50)," [Online]. Available at: http://www.wavetekmeterman.com/mmusen/products/MM+LCR55+CR50.htm?catalog_name=MetermanUnitedStates (2011) (accessed January 11, 2012).
31. M. Motor, "RE-max 17, 17mm, 4 Watt," [Online]. Available at: http://shop.maxonmotor.com/ishop/article/article/214897.xml (2011) (accessed December 20, 2011).

32. A. J. Ijspeert, *Improvement of the Cheetah Locomotion Control*. Master Project. EPFL [Online]. Available at: Biorobotics Laboratory BIOROB (2010).
33. E. Schuitema, M. Wisse, T. Ramakers and P. Jonker, "The Design of Leo: A 2d Bipedal Walking Robot for Online Autonomous Reinforcement Learning," *Intelligent Robots and Systems (IROS), 2010 IEEE/RSJ International Conference on*, IEEE (2010) pp. 3238–3243.
34. R. Inc., "Robotis e-manual v1.08.00," [Online]. Available at: http://support.robotis.com/en/ (2011) (accessed Dec. 20, 2011).
35. L. Robotis CO., "Robotis user's manual dynamixel rx-28 v1.10," [Online]. Available at: http://www.crustcrawler.com/motors/RX28/docs/RX28_Manual.pdf (2011) (accessed Jan. 20, 2012).
36. T.-S. Dao and J. McPhee, "Dynamic modeling of electrochemical systems using linear graph theory," *J. Power Sources* **196**(23), 10 442–10 454 (2011).
37. Maplesoft, "Maplesim model gallery," http://www.maplesoft.com/products/maplesim/modelgallery/ (accessed September 30, 2012).
38. J. Donelan, Q. Li, V. Naing, J. Hoffer, D. Weber and A. Kuo, "Biomechanical energy harvesting: generating electricity during walking with minimal user effort," *Science*, **319**(5864), 807–810 (2008).
39. Q. Li, V. Naing, J. Hoffer, D. Weber, A. Kuo and J. Donelan, "Biomechanical Energy Harvesting: Apparatus and Method," *Robotics and Automation, 2008. ICRA 2008. IEEE International Conference on*, IEEE (2008) pp. 3672–3677.
40. R. Riemer and A. Shapiro,"Biomechanical energy harvesting from human motion: Theory, state of the art, design guidelines, and future directions," *J. Neuroengineering Rehabil.* **8**(1), 22 (2011).
41. N.G. Elvin and A.A. Elvin,"Vibrational energy harvesting from human gait," *IEEE* **18**(2), 637 (2013).
42. H. Huang, G. V. Merrett and N. M. White,"Human-powered inertial energy harvesters: The effect of orientation, location and activity on obtainable power," *Procedia Eng.* **25**, 815–818 (2011).
43. R. D. Kornbluh, R. Pelrine, H. Prahlad, A. Wong-Foy, B. McCoy, S. Kim, J. Eckerle and T. Low, "Stretching the Capabilities of Energy Harvesting: Electroactive Polymers Based on Dielectric Elastomers," *Advances in Energy Harvesting Methods* (2013) pp. 399–415.
44. M. Gorlatova, J. Sarik, M. Cong, I. Kymissis and G. Zussman, "Movers and Shakers: Kinetic Energy Harvesting for the Internet of Things," *arXiv preprint arXiv: 1307.0044* (2013).
45. P. L. Green, E. Papatheou and N. D. Sims, "Energy harvesting from human motion: An evaluation of current nonlinear energy harvesting solutions," *J. Phys.: Conf. Ser.* **382**(1), 012023 (2012).
46. E. Papatheou, P. Green, V. Racic, J. M. W. Brownjohn and N. D. Sims, "A Short Investigation of the Effect of an Energy Harvesting Backpack on the Human Gait," *SPIE Smart Structures and Materials+ Nondestructive Evaluation and Health Monitoring* (2012) pp. 83410F–83410F.
47. T. C. Hou, Y. Yang, H. Zhang, J. Chen, L. J. Chen and Z. Lin Wang, "Triboelectric nanogenerator built inside shoe insole for harvesting walking energy," *Nano Energy* **2**(5), 856–862 (2013).
48. M. D. Berkemeier and R. Fearing, "Tracking fast inverted trajectories of the underactuated acrobot," *IEEE Trans. Robot. Autom.* **15**(4), 740–750 (1999).

A. Sit-to-Stand Dynamic Model

This section details the expanded form of the matrix and vector elements in Eqs. (2)–(4). The mass matrix in Eq. (2) is

$$\boldsymbol{M}(\boldsymbol{\theta}) = \begin{bmatrix} \alpha_1 & \alpha_2 & \alpha_3 \\ \beta_1 & \beta_2 & \beta_3 \\ \gamma_1 & \gamma_2 & \gamma_3 \end{bmatrix}.$$

The first row of the mass matrix is made up of three terms: α_1,α_2 and α_3. The first row of these, α_1 is

$$\begin{aligned} \alpha_1 = {} & m_3 l_{31}^2 + l_{22}^2 m_3 + m_2 l_{21}^2 \\ & + m_3 l_{21}^2 + l_{11}^2 m_2 + l_{12}^2 m_2 \\ & + l_{11}^2 m_1 + l_{12}^2 m_3 + l_{11}^2 m_3 \\ & + 2\, l_{31} m_3 \cos(\theta_3(t)) l_{21} + 2\, l_{11} m_3 l_{22} \cos(\theta_2(t)) \\ & + 2\, l_{11} m_3 l_{21} \cos(\theta_2(t)) + 2\, l_{11} m_2 l_{21} \cos(\theta_2(t)) \\ & + 2\, l_{12} m_3 l_{22} \cos(\theta_2(t)) + 2\, l_{12} m_3 l_{21} \cos(\theta_2(t)) \\ & + 2\, l_{12} m_2 l_{21} \cos(\theta_2(t)) + 2\, l_{31} m_3 \cos(\theta_3(t)) l_{22} \end{aligned}$$

https://doi.org/10.1017/S026357471400006X Published online by Cambridge University Press

$$
\begin{aligned}
&+2\,l_{22}m_3l_{21}+2\,l_{11}m_2l_{12}+2\,l_{11}m_3l_{12}\\
&+2\,l_{31}\cos(\theta_2(t))\cos(\theta_3(t))m_3l_{11}+2\,l_{31}\cos(\theta_2(t))\cos(\theta_3(t))m_3l_{12}\\
&-2\,l_{31}\sin(\theta_2(t))\sin(\theta_3(t))m_3l_{11}-2\,l_{31}\sin(\theta_2(t))\sin(\theta_3(t))m_3l_{12}\\
&+Izz_{shank}+Izz_{hat}+Izz_{thigh}
\end{aligned}
\tag{15}
$$

the second term, α_2 is

$$
\begin{aligned}
\alpha_2 = {}& l_{11}m_3l_{22}\cos(\theta_2(t))+l_{11}m_3l_{21}\cos(\theta_2(t))\\
&+l_{11}m_2l_{21}\cos(\theta_2(t))+l_{12}m_3l_{22}\cos(\theta_2(t))\\
&+l_{12}m_3l_{21}\cos(\theta_2(t))+l_{12}m_2l_{21}\cos(\theta_2(t))\\
&+2\,l_{31}m_3\cos(\theta_3(t))l_{22}+2\,l_{31}m_3\cos(\theta_3(t))l_{21}\\
&+2\,l_{22}m_3l_{21}+\,l_{31}\cos(\theta_2(t))\cos(\theta_3(t))m_3l_{11}+l_{31}\cos(\theta_2(t))\cos(\theta_3(t))m_3l_{12}\\
&-l_{31}\sin(\theta_2(t))\sin(\theta_3(t))m_3l_{11}-l_{31}\sin(\theta_2(t))\sin(\theta_3(t))m_3l_{12}\\
&+Izz_{hat}+Izz_{thigh}+\,l_{22}^2m_3+m_2l_{21}^2+\,m_3{l_{21}}^2+m_3l_{31}^2
\end{aligned}
\tag{16}
$$

and the third term α_3 is

$$
\begin{aligned}
\alpha_3 = {}& l_{31}m_3\cos(\theta_3(t))l_{22}+l_{31}m_3\cos(\theta_3(t))l_{21}\\
&+l_{31}\cos(\theta_2(t))\cos(\theta_3(t))m_3l_{11}+l_{31}\cos(\theta_2(t))\cos(\theta_3(t))m_3l_{12}\\
&-l_{31}\sin(\theta_2(t))\sin(\theta_3(t))m_3l_{11}-l_{31}\sin(\theta_2(t))\sin(\theta_3(t))m_3l_{12}\\
&+Izz_{hat}+m_3l_{31}^2.
\end{aligned}
\tag{17}
$$

The second row of the mass matrix is also made up of three terms: β_1,β_2 and β_3. The first term, β_1 is

$$
\begin{aligned}
\beta_1 = {}& l_{11}m_3l_{22}\cos(\theta_2(t))+l_{11}m_3l_{21}\cos(\theta_2(t))\\
&+l_{11}m_2l_{21}\cos(\theta_2(t))+l_{12}m_3l_{22}\cos(\theta_2(t))\\
&+l_{12}m_3l_{21}\cos(\theta_2(t))+l_{12}m_2l_{21}\cos(\theta_2(t))\\
&+2\,l_{31}m_3\cos(\theta_3(t))l_{22}+2\,l_{31}m_3\cos(\theta_3(t))l_{21}\\
&+2\,l_{22}m_3l_{21}+\,l_{31}\cos(\theta_2(t))\cos(\theta_3(t))m_3l_{11}+l_{31}\cos(\theta_2(t))\cos(\theta_3(t))m_3l_{12}\\
&-l_{31}\sin(\theta_2(t))\sin(\theta_3(t))m_3l_{11}-l_{31}\sin(\theta_2(t))\sin(\theta_3(t))m_3l_{12}\\
&+Izz_{hat}+Izz_{thigh}+\,l_{22}^2m_3+m_2l_{21}^2+\,m_3l_{21}^2+m_3l_{31}^2
\end{aligned}
\tag{18}
$$

while the second term, β_2 is

$$
\begin{aligned}
\beta_2 = {}& 2\,l_{31}m_3\cos(\theta_3(t))l_{22}+2\,l_{31}m_3\cos(\theta_3(t))l_{21}+2\,l_{22}m_3l_{21}\\
&+Izz_{hat}+Izz_{thigh}+l_{22}^2m_3\\
&+m_2l_{21}^2+m_3l_{21}^2+m_3l_{31}^2
\end{aligned}
\tag{19}
$$

and the third term, β_3 is

$$
\beta_3 = l_{31}m_3\cos(\theta_3(t))l_{22}+l_{31}m_3\cos(\theta_3(t))l_{21}+Izz_{hat}+m_3l_{31}^2. \tag{20}
$$

https://doi.org/10.1017/S026357471400006X Published online by Cambridge University Press

Finally, the last row of the mass matrix is made up of three terms: γ_1, γ_2 and γ_3. The first term, γ_1 is

$$\begin{aligned}\gamma_1 = {} & l_{31} m_3 \cos(\theta_3(t)) l_{22} + l_{31} m_3 \cos(\theta_3(t)) l_{21} \\ & + l_{31} \cos(\theta_2(t)) \cos(\theta_3(t)) m_3 l_{11} + l_{31} \cos(\theta_2(t)) \cos(\theta_3(t)) m_3 l_{12} \\ & - l_{31} \sin(\theta_2(t)) \sin(\theta_3(t)) m_3 l_{11} - l_{31} \sin(\theta_2(t)) \sin(\theta_3(t)) m_3 l_{12} \\ & + Izz_{hat} + m_3 l_{31}^2 \end{aligned} \tag{21}$$

the second term, γ_2 is

$$\gamma_2 = l_{31} m_3 \cos(\theta_3(t)) l_{22} + l_{31} m_3 \cos(\theta_3(t)) l_{21} + Izz_{hat} + m_3 l_{31}^2 \tag{22}$$

and the third term, γ_3 is

$$\gamma_3 = Izz_{hat} + m_3 l_{31}^2. \tag{23}$$

The 3 x 1 Coriolis and centrifugal vector in Eq. (3) is

$$\boldsymbol{V}(\boldsymbol{\theta}, \dot{\boldsymbol{\theta}}) = [\delta_1 \;\; \delta_2 \;\; \delta_3]^T.$$

The Coriolis and centrifugal components contain three terms: δ_1, δ_2 and δ_3. The first term, δ_1 is

$$\begin{aligned}\delta_1 = {} & 2 l_{11} m_2 l_{21} \left(\frac{d}{dt}\theta_1(t)\right)\left(\frac{d}{dt}\theta_2(t)\right) \sin(\theta_2(t)) \\ & + 2 l_{12} m_3 l_{22} \left(\frac{d}{dt}\theta_1(t)\right)\left(\frac{d}{dt}\theta_2(t)\right) \sin(\theta_2(t)) \\ & + 2 l_{12} m_3 l_{21} \left(\frac{d}{dt}\theta_1(t)\right)\left(\frac{d}{dt}\theta_2(t)\right) \sin(\theta_2(t)) \\ & + 2 l_{12} m_2 l_{21} \left(\frac{d}{dt}\theta_1(t)\right)\left(\frac{d}{dt}\theta_2(t)\right) \sin(\theta_2(t)) \\ & + 2 l_{11} m_3 l_{21} \left(\frac{d}{dt}\theta_1(t)\right)\left(\frac{d}{dt}\theta_2(t)\right) \sin(\theta_2(t)) \\ & + 2 l_{21} m_3 l_{31} \left(\frac{d}{dt}\theta_2(t)\right)\left(\frac{d}{dt}\theta_3(t)\right) \sin(\theta_3(t)) \\ & + 2 l_{21} m_3 l_{31} \left(\frac{d}{dt}\theta_1(t)\right)\left(\frac{d}{dt}\theta_3(t)\right) \sin(\theta_3(t)) \\ & + 2 l_{22} m_3 l_{31} \left(\frac{d}{dt}\theta_2(t)\right)\left(\frac{d}{dt}\theta_3(t)\right) \sin(\theta_3(t)) \\ & + 2 l_{11} m_3 l_{22} \left(\frac{d}{dt}\theta_1(t)\right)\left(\frac{d}{dt}\theta_2(t)\right) \sin(\theta_2(t)) \\ & + 2 l_{22} m_3 l_{31} \left(\frac{d}{dt}\theta_1(t)\right)\left(\frac{d}{dt}\theta_3(t)\right) \sin(\theta_3(t)) \\ & + 2 l_{11} m_3 l_{31} \left(\frac{d}{dt}\theta_1(t)\right)\left(\frac{d}{dt}\theta_2(t)\right) \cos(\theta_2(t)) \sin(\theta_3(t)) \\ & + 2 l_{11} m_3 l_{31} \left(\frac{d}{dt}\theta_1(t)\right)\left(\frac{d}{dt}\theta_3(t)\right) \cos(\theta_2(t)) \sin(\theta_3(t)) \end{aligned}$$

https://doi.org/10.1017/S026357471400006X Published online by Cambridge University Press

$$+2\,l_{11}m_3l_{31}\left(\frac{d}{dt}\theta_2(t)\right)\left(\frac{d}{dt}\theta_3(t)\right)\sin(\theta_2(t))\cos(\theta_3(t))$$

$$+2\,l_{12}m_3l_{31}\left(\frac{d}{dt}\theta_1(t)\right)\left(\frac{d}{dt}\theta_3(t)\right)\cos(\theta_2(t))\sin(\theta_3(t))$$

$$+2\,l_{11}m_3l_{31}\left(\frac{d}{dt}\theta_1(t)\right)(\frac{d}{dt}\theta_2(t))\sin(\theta_2(t))\cos(\theta_3(t))$$

$$+2\,l_{11}m_3l_{31}\left(\frac{d}{dt}\theta_1(t)\right)\left(\frac{d}{dt}\theta_3(t)\right)\sin(\theta_2(t))\cos(\theta_3(t))$$

$$+2\,l_{11}m_3l_{31}\left(\frac{d}{dt}\theta_2(t)\right)\left(\frac{d}{dt}\theta_3(t)\right)\cos(\theta_2(t))\sin(\theta_3(t))$$

$$+2\,l_{12}m_3l_{31}\left(\frac{d}{dt}\theta_1(t)\right)\left(\frac{d}{dt}\theta_2(t)\right)\cos(\theta_2(t))\sin(\theta_3(t))$$

$$+2\,l_{12}m_3l_{31}\left(\frac{d}{dt}\theta_1(t)\right)\left(\frac{d}{dt}\theta_2(t)\right)\sin(\theta_2(t))\cos(\theta_3(t))$$

$$+2\,l_{12}m_3l_{31}\left(\frac{d}{dt}\theta_1(t)\right)\left(\frac{d}{dt}\theta_3(t)\right)\sin(\theta_2(t))\cos(\theta_3(t))$$

$$+2\,l_{12}m_3l_{31}\left(\frac{d}{dt}\theta_2(t)\right)\left(\frac{d}{dt}\theta_3(t)\right)\cos(\theta_2(t))\sin(\theta_3(t))$$

$$+2\,l_{12}m_3l_{31}\left(\frac{d}{dt}\theta_2(t)\right)\left(\frac{d}{dt}\theta_3(t)\right)\sin(\theta_2(t))\cos(\theta_3(t))$$

$$+l_{12}m_3l_{31}\left(\frac{d}{dt}\theta_2(t)\right)^2\cos(\theta_2(t))\sin(\theta_3(t))$$

$$+l_{12}m_3l_{31}\left(\frac{d}{dt}\theta_2(t)\right)^2\sin(\theta_2(t))\cos(\theta_3(t))$$

$$+l_{12}m_3l_{31}\left(\frac{d}{dt}\theta_3(t)\right)^2\cos(\theta_2(t))\sin(\theta_3(t))$$

$$+l_{12}m_3l_{31}\left(\frac{d}{dt}\theta_3(t)\right)^2\sin(\theta_2(t))\cos(\theta_3(t))$$

$$+l_{11}m_3l_{31}\left(\frac{d}{dt}\theta_2(t)\right)^2\sin(\theta_2(t))\cos(\theta_3(t))$$

$$+l_{11}m_3l_{31}\left(\frac{d}{dt}\theta_2(t)\right)^2\cos(\theta_2(t))\sin(\theta_3(t))$$

$$+l_{11}m_3l_{31}\left(\frac{d}{dt}\theta_3(t)\right)^2\cos(\theta_2(t))\sin(\theta_3(t))$$

$$+l_{11}m_3l_{31}\left(\frac{d}{dt}\theta_3(t)\right)^2\sin(\theta_2(t))\cos(\theta_3(t))$$

$$+l_{22}m_3l_{31}\left(\frac{d}{dt}\theta_3(t)\right)^2\sin(\theta_3(t))+l_{21}m_3l_{31}\left(\frac{d}{dt}\theta_3(t)\right)^2\sin(\theta_3(t))$$

$$+l_{11}m_3l_{22}\left(\frac{d}{dt}\theta_2(t)\right)^2\sin(\theta_2(t))+l_{12}m_3l_{22}\left(\frac{d}{dt}\theta_2(t)\right)^2\sin(\theta_2(t))$$

https://doi.org/10.1017/S026357471400006X Published online by Cambridge University Press

$$+ l_{12} m_3 l_{21} \left(\frac{d}{dt}\theta_2(t)\right)^2 \sin(\theta_2(t)) + l_{12} m_2 l_{21} \left(\frac{d}{dt}\theta_2(t)\right)^2 \sin(\theta_2(t))$$
$$+ l_{11} m_3 l_{21} \left(\frac{d}{dt}\theta_2(t)\right)^2 \sin(\theta_2(t)) l_{11} m_2 l_{21} \left(\frac{d}{dt}\theta_2(t)\right)^2 \sin(\theta_2(t)) \tag{24}$$

the second term, δ_2 is

$$\begin{aligned}
\delta_2 = {} & 2\, l_{21} m_3 l_{31} \left(\frac{d}{dt}\theta_2(t)\right)\left(\frac{d}{dt}\theta_3(t)\right)\sin(\theta_3(t)) \\
& + 2\, l_{21} m_3 l_{31} \left(\frac{d}{dt}\theta_1(t)\right)\left(\frac{d}{dt}\theta_3(t)\right)\sin(\theta_3(t)) \\
& + 2\, l_{22} m_3 l_{31} \left(\frac{d}{dt}\theta_2(t)\right)\left(\frac{d}{dt}\theta_3(t)\right)\sin(\theta_3(t)) \\
& + 2\, l_{22} m_3 l_{31} \left(\frac{d}{dt}\theta_1(t)\right)\left(\frac{d}{dt}\theta_3(t)\right)\sin(\theta_3(t)) \\
& - l_{31} m_3 \cos(\theta_2(t))\sin(\theta_3(t)) \left(\frac{d}{dt}\theta_1(t)\right)^2 l_{12} \\
& - l_{31} m_3 \cos(\theta_2(t))\sin(\theta_3(t)) \left(\frac{d}{dt}\theta_1(t)\right)^2 l_{11} \\
& - l_{31} m_3 \sin(\theta_2(t))\cos(\theta_3(t)) \left(\frac{d}{dt}\theta_1(t)\right)^2 l_{12} \\
& - l_{31} m_3 \sin(\theta_2(t))\cos(\theta_3(t)) \left(\frac{d}{dt}\theta_1(t)\right)^2 l_{11} \\
& + l_{22} m_3 l_{31} \left(\frac{d}{dt}\theta_3(t)\right)^2 \sin(\theta_3(t)) + l_{21} m_3 l_{31} \left(\frac{d}{dt}\theta_3(t)\right)^2 \sin(\theta_3(t)) \\
& - l_{11} m_3 l_{22} \left(\frac{d}{dt}\theta_1(t)\right)^2 \sin(\theta_2(t)) - l_{11} m_3 l_{21} \left(\frac{d}{dt}\theta_1(t)\right)^2 \sin(\theta_2(t)) \\
& - l_{11} m_2 l_{21} \left(\frac{d}{dt}\theta_1(t)\right)^2 \sin(\theta_2(t)) - l_{12} m_3 l_{22} \left(\frac{d}{dt}\theta_1(t)\right)^2 \sin(\theta_2(t)) \\
& - l_{12} m_3 l_{21} \left(\frac{d}{dt}\theta_1(t)\right)^2 \sin(\theta_2(t)) - l_{12} m_2 l_{21} \left(\frac{d}{dt}\theta_1(t)\right)^2 \sin(\theta_2(t))
\end{aligned} \tag{25}$$

and the third term, δ_3 is

$$\begin{aligned}
\delta_3 = {} & -2\, l_{31} \sin(\theta_3(t)) m_3 l_{21} \left(\frac{d}{dt}\theta_1(t)\right)\frac{d}{dt}\theta_2(t) - 2\, l_{31} \sin(\theta_3(t)) m_3 l_{22} \left(\frac{d}{dt}\theta_1(t)\right)\frac{d}{dt}\theta_2(t) \\
& - l_{31} m_3 \cos(\theta_2(t))\sin(\theta_3(t)) \left(\frac{d}{dt}\theta_1(t)\right)^2 l_{12} - l_{31} m_3 \cos(\theta_2(t))\sin(\theta_3(t)) \left(\frac{d}{dt}\theta_1(t)\right)^2 l_{11} \\
& - l_{31} m_3 \sin(\theta_2(t))\cos(\theta_3(t)) \left(\frac{d}{dt}\theta_1(t)\right)^2 l_{12} - l_{31} m_3 \sin(\theta_2(t))\cos(\theta_3(t)) \left(\frac{d}{dt}\theta_1(t)\right)^2 l_{11}
\end{aligned}$$

https://doi.org/10.1017/S026357471400006X Published online by Cambridge University Press

$$- l_{31}\sin(\theta_3(t))m_3 l_{22}\left(\frac{d}{dt}\theta_1(t)\right)^2 - l_{31}\sin(\theta_3(t))m_3 l_{22}\left(\frac{d}{dt}\theta_2(t)\right)^2$$
$$- l_{31}\sin(\theta_3(t))m_3 l_{21}\left(\frac{d}{dt}\theta_1(t)\right)^2 - l_{31}\sin(\theta_3(t))m_3 l_{21}\left(\frac{d}{dt}\theta_2(t)\right)^2. \quad (26)$$

The 3×1 vector of gravitational components in Eq. (4) is

$$\boldsymbol{G}(\boldsymbol{\theta}) = [\zeta_1 \;\; \zeta_2 \;\; \zeta_3]^T,$$

where the gravitational components are composed of three terms: ζ_1, ζ_2 and ζ_3. The first term, ζ_1 is

$$\begin{aligned}\zeta_1 = {} & \sin(\theta_1(t))l_{11}gm_3 + \sin(\theta_1(t))l_{11}gm_1 + \sin(\theta_1(t))l_{11}gm_2 + \sin(\theta_1(t))l_{12}gm_3 \\ & + l_{31}\cos(\theta_1(t))\cos(\theta_2(t))\sin(\theta_3(t))gm_3 + l_{31}\cos(\theta_1(t))\sin(\theta_2(t))\cos(\theta_3(t))gm_3 \\ & - l_{31}\sin(\theta_1(t))\sin(\theta_2(t))\sin(\theta_3(t))gm_3 + l_{31}\sin(\theta_1(t))\cos(\theta_2(t))\cos(\theta_3(t))gm_3 \\ & + l_{22}\cos(\theta_1(t))\sin(\theta_2(t))gm_3 + l_{22}\sin(\theta_1(t))\cos(\theta_2(t))gm_3 \\ & + l_{21}\cos(\theta_1(t))\sin(\theta_2(t))gm_3 + l_{21}\sin(\theta_1(t))\cos(\theta_2(t))gm_3 \\ & + l_{21}\cos(\theta_1(t))\sin(\theta_2(t))gm_2 + l_{21}\sin(\theta_1(t))\cos(\theta_2(t))gm_2 \\ & + \sin(\theta_1(t))l_{12}gm_2 \end{aligned} \quad (27)$$

the second term, ζ_2 is

$$\begin{aligned}\zeta_2 = {} & l_{31}\cos(\theta_1(t))\cos(\theta_2(t))\sin(\theta_3(t))gm_3 \\ & + l_{31}\cos(\theta_1(t))\sin(\theta_2(t))\cos(\theta_3(t))gm_3 \\ & - l_{31}\sin(\theta_1(t))\sin(\theta_2(t))\sin(\theta_3(t))gm_3 \\ & + l_{31}\sin(\theta_1(t))\cos(\theta_2(t))\cos(\theta_3(t))gm_3 \\ & + l_{22}\cos(\theta_1(t))\sin(\theta_2(t))gm_3 + l_{22}\sin(\theta_1(t))\cos(\theta_2(t))gm_3 \\ & + l_{21}\cos(\theta_1(t))\sin(\theta_2(t))gm_3 + l_{21}\sin(\theta_1(t))\cos(\theta_2(t))gm_3 \\ & + l_{21}\cos(\theta_1(t))\sin(\theta_2(t))gm_2 + l_{21}\sin(\theta_1(t))\cos(\theta_2(t))gm_2 \end{aligned} \quad (28)$$

and the third term, ζ_3 is

$$\begin{aligned}\zeta_3 = {} & l_{31}\cos(\theta_1(t))\cos(\theta_2(t))\sin(\theta_3(t))gm_3 \\ & + l_{31}\cos(\theta_1(t))\sin(\theta_2(t))\cos(\theta_3(t))gm_3 \\ & + l_{31}\sin(\theta_1(t))\cos(\theta_2(t))\cos(\theta_3(t))gm_3 \\ & - l_{31}\sin(\theta_1(t))\sin(\theta_2(t))\sin(\theta_3(t))gm_3. \end{aligned} \quad (29)$$

https://doi.org/10.1017/S026357471400006X Published online by Cambridge University Press